

# Morphological environment survey and hydrodynamic modeling of a large bifurcation-confluence complex in Yangtze River, China

Liu Tong-Huan<sup>1,2</sup>, Wang Xie-Kang<sup>2</sup>, Duan Huan-Feng<sup>3</sup>, Yan Xu-Feng<sup>2,\*</sup>

1 Changjiang River Scientific Research Institute, Wuhan, China

2 State Key Laboratory of Hydraulics and Mountain River Engineering, Sichuan University, Chengdu, China

3 Department of Civil and Environmental Engineering, The Hong Kong Polytechnic University, Hong Kong SAR, China

## Abstract

Since the establishment of the world-class Three Gorges Dam (TGD) across the Yangtze River, China, the downstream reach has experienced a long-term adjustment with regard to the river morphology and hydrodynamics, imposing a profound impact on the conditions of human living and aquatic ecosystem. This study presents an investigation on the river channel morphological characteristics and hydrodynamic environment of a large bifurcation-confluence complex downstream the TGD through detailed field survey and numerical modeling. Results show that the main stem, before being bifurcated into two sub-channels (North and South channels), experiences a meander, leading to the severe bed scouring near the outer bank (pools) resulted from a high flow mass flux and bed shear stress. Because of being bifurcated, the river width with largely growing may result in the reduction of flow velocity and sediment deposition (riffles), and thereby two plugbars are formed near the entrance of two sub-channels. In the meantime, velocity-reversal phenomenon (flow velocity and friction velocity) is identified when low flows are transited into high flows. The results also reveal that the flow mass flux is always larger in pool regions, which is

highly related to water depth. As a result, the topographic steering of flows by riffles, bars and floodplains may have more impact on flow path under low flow conditions, while the bankline shape would become more important under high flows. Furthermore, the topographic steering could play a key role in the pattern of flow separations near the confluence. More interestingly, the confluence flow separation only occurs under low flow conditions and its occurring location shifts upwards the tributary (North channel), which differs from observations in previous studies. The visualized numerical results of friction velocity distribution indicate that sediment is more likely to deposit in the North channel (entrance) with lower friction velocity, implying the potential closure of the sub-channel.

Keyword: Bifurcation-confluence, River center bar, Topographic steering, Flow separation, Discharge ratio.

## **1 Introduction**

Human activities influence the environment of various perspectives. The installation of dams on rivers has profound impact on dynamics of flows, sediment and morphology for both upstream (Xu, 1989) and downstream (Graf, 2006). With respect to the latter, a dam can largely deflect sediment loads from upstream, which play a significant role in shaping river morphology (e.g. bank and bed). Since the world-class high-volume waterpower dam, the Three Gorges Dam (TGD), was constructed on the Yangtze River, the downstream reach has been undergoing a variety of hydromorphological adjustments such as width variations, channel degradations, thalweg wanderings and updates of sediment bars, pools and riffles (Brandt, 2000; Lyu et al., 2018; Ma et al., 2012; Provansal et al., 2014). Thus, the hydrodynamics responsible for the modification of river

morphology is likely to be changed significantly, resulting in lots of uncertainties for human living (Brandt, 2000; Lyu et al., 2018; Zhou et al., 2017) and aquatic species rehabilitation (Hassan and Woodsmith, 2004; Schmidt and Wilcock, 2008; Yi et al., 2013).

River bars or islands are the results of temporal and spatial variabilities of water flow and sediment transport of upstream inflows (Garcia and Niño, 1993; Tubino et al., 1999; Wu and Yeh, 2005).

River bars can be divided into two categories in accordance with the pattern of bar dynamics, referred to as free bars and forced bars (Seminara and Tubino, 1989). The former kind commonly spontaneously occurs in relatively straight reaches, such as braided rivers (Tubino et al., 1999), which is induced by bed topography instability owing to flow-sediment interaction. The latter kind is mainly attributed to boundary constriction of rivers and channels. Unlike free bars which form and diminish periodically, forced bars are fairly steady and non-migrating, consequently leading to the formation of stable bifurcation (Wu and Yeh, 2005). With a forced bar occupying partly the river bed, the upstream inflow first diverges into two branches around the bar and then converges into a main flow again. Therefore, the entire flow process can be interpreted as flow through a bifurcation and then a confluence, respectively (Szupiany et al., 2009; Zinger et al., 2013), characterized by two typical dynamics of flow and sediment.

For a single bifurcation, the upstream incoming flow and sediment in the single upstream main channel is partitioned into a two-channel system. In natural scenarios, river bars are commonly coincident with an upstream meander. In this case, flow initially moves in the transverse direction in the upstream meander, leading to apparent helical motions and thus transverse sediment transport. This further affects the distinguished evolution of the bed topography of the two-channel system and flow-sediment partitioning processes (Hackney et al., 2018; Thomas et al., 2011) and make the

bifurcation problem more complex in terms of both hydro- and morpho- dynamics (Hardy et al., 2011; Van Denderen et al., 2018). For a confluence, two streams join together, transforming into a shear flow evolving downstream. Against the shear face, flows tend to become unstable, forming large-scale coherent vortices and facilitating the mixing of the two streams (Best and Reid, 1984; Biron et al., 1996; Yang et al., 2009). Moreover, on the side of the tributary, a flow separation zone can occur when the tributary stream injects the main stream with an angle, effectively trapping sediment and pollutants. The features of both flow mixing and separation are dominantly determined by the discharge ratio of main stream to tributary stream (Liu et al., 2012; Yang et al., 2009). On contrary to a simple confluence channel system, the hydro- and morph-dynamics arising from the upstream bifurcation would have critical impacts on the dynamics of flow, sediment and morphology at the subsequent confluence when flow exits the divergence-confluence unit. On one hand, the discharge ratio of main stream to tributary is controlled by the bifurcation flow partitioning. On the other hand, bed morphological change due to sediment dynamics influenced by the bifurcation establishes non-uniform bottom form roughness near the confluence. Both above perspectives essentially affect the confluence hydrodynamics, e.g. the scale and geometry of flow separation and shear flow mixing. A further speculation is that the evolved hydrodynamics at the downstream confluence would inversely influence the upstream bifurcation such as the stability. Therefore, the two structures are highly correlated to each other in a bifurcation-confluence complex.

Previous studies have documented investigations of a large-scale bifurcation-confluence complex in a natural river except the following several studies. Parsons et al. (2007) based on field-survey data investigated the bed morphology and 3D flow structure in a bifurcation-confluence complex in a

straight width-varied reach. The target has a very large scale with the ratio of width to depth (aspect ratio) being as large as 200, in contrast to some small rivers with aspect ratio less than 50. Zinger et al. (2013) examined the flow structure and bed morphology of two developing chute cutoffs on a single meander bend. The authors identified characteristic flow hydrodynamics and bed morphology at different locations of bifurcation and confluence. The study indicates the essential nature between hydrodynamics and morphodynamics in a bifurcation-confluence complex. Hackney et al. (2018) also used field survey data to analyze 3D hydrodynamics and morphology pattern of a bifurcation-confluence complex in a large-scale river but with meandering banks. The survey data included three flow conditions (rising limb flow, highest flow and falling limb flow) in a full hydrograph in 10 months. Their study reported that the island (bar) complex acted as a net sink of sediment during the highest flow while maintained a quasi-equilibrium state during the two limb flows. It was shown that the discharge asymmetry of bifurcation was controlled by water discharge and bed morphological change. Le et al. (2018) conducted large-eddy simulation (LES) to investigate the bifurcation-confluence flow over an equilibrium (unchanged without high flows) bed bathymetry in a 3.2km long, relatively straight reach of the Mississippi River. The simulation, not considering sediment motion and bed morphological change, successfully demonstrated the insight into the understanding of the river flow dynamics (i.e. velocities, vorticity, turbulent kinetic energy) dominated by the interaction of shear-layers arising from islands and bars.

The above studies are on hydrodynamics and morphodynamics of a bifurcation-confluence complex without the limitation of upstream sediment supply. The gained knowledge, however, might not be applicable when a dam is constructed upstream. This study, therefore, focuses on a large-scale bifurcation-confluence complex induced by a river center bar in the Yangtze River, at upstream of

which the TGD largely limits the downstream sediment load rate. To fulfill this goal, (1) a high-resolution river morphology measurement was made to demonstrate morphological characteristics of the bifurcation-confluence complex; (2) a hydrodynamic model was used to simulate flow in the bifurcation-confluence complex and field measured results were used to check the model performance; (3) based on the known bed morphology, varying flow stages were adopted into the hydrodynamic model to investigate the hydrodynamics of the bifurcation-confluence complex under flow varying from low to high; and (4) a comparison that between the present results with respect to the current bifurcation-confluence complex and other studies were made in discussion.

## **2 Study site and methods**

### **2.1 Field site**

The study site named Heishazhou is located in the middle and lower reach of The Yangtze River in Anhui Province, China as shown in Figure 1a. The site is located ~ 500 km downstream the Three Gorges Dam (TGD), the construction of which was initiated in 1994 and completed in 2003. A large-scale (forced) river bar (bar area ~ 35.4 km<sup>2</sup>) centers in the main stem to form a bifurcation at the bar head and a confluence at the bar trail (Figure 1b). Since the last contrary, the sediment transport discharge of the target reach has been decreasing by field observations (4.70×10<sup>9</sup> ton/year for 1951-1985, 3.40×10<sup>9</sup> ton/year for 1986-2002 and 1.37×10<sup>9</sup> ton/year for 2003-2015 ) (Niu et al., 2017). In particular, with the construction of the TGD, a further decrease in sediment transport discharge was observed, which is attributed to the trapping effect of the upstream sediment by the dam. Field site survey showed that annual bed erosion (erosion rate ~ 2.44×10<sup>9</sup> t. yr<sup>-1</sup>) occurred at

the reach on average before the dam construction (1981-2001). After the dam storing water (2001-2006), bed erosion was further enhanced (erosion rate  $\sim 4.35 \times 10^{10}$  t. yr<sup>-1</sup>). However, a sharp drop of bed erosion was observed during 2006-2011 (erosion rate  $\sim 6.68 \times 10^9$  t. yr<sup>-1</sup>). Recently (2011-2016), sediment deposition dominated the change of the bed topography (deposition rate  $\sim 6.68 \times 10^9$  t. yr<sup>-1</sup>). Though the low-sediment-concentration water released from the dam has the ability to erode more sediment from the downstream reach, the downstream sediment activity still has been becoming increasingly weak, which significantly affects the processes of the downstream river morphology by variations of erosion and deposition (e.g. width and bathymetry) (Xia et al., 2017; Yang et al., 2014).

Prior to the bifurcation, a meander with the radius  $\sim 5.7$ km exists (Figure 1b), allowing secondary flows to develop before entering the bar region. The secondary flow structure is expected to be able to affect the partitioning of water flows and sediment loads in the two sub-channels (Van Denderen et al., 2018). Because of human activities, the regulation of river banklines has been made to prevent bank erosion to maintain the bifurcation-confluence complex. Therefore, the morphological change of the river can be considered the variation of the bed topography only. Moreover, because of the function of navigation, regular bed sediment dredging is made for waterway maintenance.



Figure 1 Geographic information of the study site (sources from ArcGIS and Google Earth).

## 2.2 Methods

### Field site measurements of morphodynamics and hydrodynamics

Two campaigns in the year of 2006 and 2016 were carried out to measure bed topography.

Topographic data were collected using a single-beam echo-sounder (SBES) HY1600 with the working frequency of 208 kHz, coupled with a differential global positioning system (dGPS). Streamwisely, topographic data were obtained along cross sections perpendicular to channel banks. A separation distance between adjacent cross sections was set  $\sim 200\text{m}$ . The measurement locations on a single cross section were determined according to the variation of the bed topography.

Flow velocities on six cross-sections (CS1-CS6) distributing uniformly over the bifurcation-convergence structure (see Figure 1b) were obtained during field surveys in order to provide fundamental data for numerical model validation. An RDI 1500 kHz ADCP was employed to measure three-dimensional flow velocities. The ADCP was installed in a moving boat at a moving speed of  $1.2\text{ ms}^{-1}$ . Over the entire water depth, six different water layers were measured to determine the depth-averaged velocity. The dGPS was also used to correct the velocity data. Velocities on a single vertical line were averaged over water depth to obtain the depth-averaged flow velocity to account for the 2D horizontal flow field. The total flow discharge at the inlet was estimated as  $\sim 14000\text{m}^3\text{s}^{-1}$  by means of integrating all velocities data over a cross-section.

## **2D hydrodynamic modelling**

This study aims to investigate hydrodynamics in a large-scale bifurcation-confluence river structure formed by a forced center river bar partitioning the Yangtze River. Of importance is depth-averaged flow velocity information around the bifurcation and confluence as well as the partitioning of water discharge by the bifurcation under different flow configurations. With the constructions of the main stem hydropower dams, the upstream sediment loads has been increasingly trapped. Furthermore, during non-flooding seasons, the river morphological change due to sediment motion can be

negligible in a short term. Therefore, a depth-averaged hydromorphological CFD code referred to as 2D solver MFlow\_02 embedded in the iRIC software is employed to fulfill the mentioned goals.

In the present study, the sediment model is not enabled due to low-sediment activities. The Reynolds stresses are determined by the Boussinesq approximation and the turbulent viscosity is modelled by a simplified  $k$ - $\varepsilon$  model, in which the turbulent kinetic energy  $k$  is calculated by bed friction velocity and water depth (Nezu and Nakagawa, 1993), and the energy dissipation rate  $\varepsilon$  is calculated by the turbulent kinetic energy (Lomax et al., 2013). Thus, the turbulent viscosity can be calculated with solving the transport equation of energy dissipation rate and turbulent energy, which largely saves the computing time. For the boundary conditions, the water discharge is adopted at the upstream inlet and the water depth is adopted as the downstream outlet. The bed friction coefficient is calculated by Manning equations with the Manning roughness coefficient in the range of 0.021-0.04  $\text{m}^{1/3}\text{s}^{-1}$ , obtained from channel roughness field surveys since 2014 (Peng et al., 2018). In this study, the Manning coefficient is set in average as 0.035  $\text{m}^{1/3}\text{s}^{-1}$ . The water surface is initially set flat at the beginning of the computation, which gradually evolves to equilibrium morphology.

The 2D solver MFlow\_02 using an unstructured grid system is capable of simulating motions of flow, sediment and bed morphology in rivers and channels with complex bank boundaries (MFlow\_02, 2018). To discretize the governing equations of flow motions, the Galerkin finite element method is used for derivatives with respect to the space and an explicit scheme is used for derivatives with respect to the time.

Unstructured triangle grid method used in this model is able to easily adapt to a river with irregular geometric boundaries. The mesh grids were automatically built in the model by setting the minimum area of elements. In particular, as the flow structure near the bifurcation and confluence is

sophisticated, the mesh grids were fined locally to capture more flow details. Specifically, the minimum area of the elements was 1000 m<sup>2</sup> and the maximum was 5000 m<sup>2</sup>. The total element number was more than 20000. The time step was set 0.5s to meet the Courant–Friedrichs–Lewy stability condition. The total computing time is set to 100000s, allowing the achievement of the fully developed flow. As a result, the CPU computing time is about 2 hours.

## **3 Results**

### **3.1 Bed morphology features**

Figure 2a shows the spatial bed morphological variation over the entire reach. It can be concluded that the bed morphology is characterized by variations of bed topography, channel width and channel curvature. Different bed forms (i.e. pools, riffles and sediment bars), as anticipated, exist in different regions over the entire bifurcation-confluence complex.

Attributed to the upstream meander, a large-scale point bar forms at the inner bank (left) near the meander apex. The maximum area of bed elevation larger than 0 exceeds ~ 35% of the entire cross-section. The bed elevation (lower than -30m) of this area reaches lowest bed topography of the entire reach, forming an elongated pool. The pool extends downstream with a distance of ~12.3 km away from the meander apex. Because of the river center bar and widen channel width (the ratio of widest width to narrowest width ~ 3.34), sediment depositing on the bed far prior to the bifurcation results in upsloping riffle bed topography.

Entering the two bifurcate sub-channels, bed elevation continuously grows because flow redistributed to two components leads to the reduction of velocity. The high-elevation bed topography forms a riffle (or plugbar) in each sub-channel, which is also observed in other studies

(Constantine et al., 2010; Zinger et al., 2013). However, it can be observed that the spatial locations of riffles differ from each other. For the south channel, sediment immediately deposits closer to the channel entrance; for the north channel, the riffle topography, however, shifts further downstream. It is interestingly noted that an elongated sediment bar is distributed along the on the left (outer) bank of the north channel with a relatively straight bankline linking the upstream reach. Similar bed morphology is not existent for the south channel, even if the turning angle of the south channel is large. As flow goes downstream of each sub-channel, the channels become re-narrowed and re-deepened. In particular for the north channel, flow experiences a sharp bend of  $\sim 130^\circ$  formed by the river bar. As a result, an elongated bar is formed on the inner bank (right) side and an elongated pool is formed on the outer bank (left) side. With a long-term alluvial process, another isolated bar (island), far smaller than the target river center bar, is formed at the bend apex near the inner bank. This smaller bar is found to be cut from the river center bar due to repeated flood circles. At the reach of the small bar, the channel width is further narrowed, resulting in a very deep pool region due to largely increased flow velocity induced by reduced channel width. At further downstream of the north channel, an elongated bar is formed on the bed of the bar side. Probably because the reach becomes sinuous before entering the confluence, another point bar is formed on the opposite side of the bar or near the right bank of the north channel. Therefore, alternate bars are formed in the downstream limb of the north channel after passing the bend apex.

The confluence is formed by the north channel perpendicularly joining the south channel. A deeply scoured pool is formed across just downstream the confluence and extends further downstream. This indicates no formation of sediment bar following the downstream corner of the confluence, which are frequently identified in the laboratory flumes and rivers (Best, 1988; Biron et al., 1996;

Zinger et al., 2013). The confluence pool gradually becomes narrowed until a distance of ~ 4km away from the confluence, and the pool region shifts toward the right side of the channel and an elongated sediment bar is developed on the left side. Particularly, it can be noted that the pool region extends upward the right side of the north channel, while on the left side sediment bar occurs.

To further understand the bed morphological characteristics, it is worthy observing the path of the channel thalweg (Figure 2b). The figure presents the evolution of thalweg path before and after the construction of the TGD. Because of the dam, upstream sediment volume is largely trapped at the dam and the downstream river reach is mainly characterized by bed scour. Meanwhile, the regular dam operation maintains the downstream reach with a less fluctuating water discharge. Clearly, the dam construction has a significant impact on bed morphological change as indicated by the thalweg path. At the reach far away from the bifurcation, the paths are closely distributed. However, the thalweg path becomes bifurcate when getting closed to the bifurcation. The path bifurcate point for Year 2016 moves much closer to the river bar and also the north channel entrance. The shifting distance of the path bifurcate points between Year 1993 and Year 2016 attains ~ 3.5km. For the north channel, the thalweg path at upstream entrance is shifted from the right bank side to the left bank side after the dam construction. When going downstream, the thalweg path for Year 1993 gradually shifts toward the right bank; conversely, the path for Year 2016 shows an opposite pattern. After the bend apex, the paths for the two years are closely aligned, shifting from the outer bank to the left bank when approaching the confluence site. For the south channel, the thalweg path keeps located in the channel middle along the entire reach for Year 1993. The path for Year 2016, however, is always aligned near the left bank at the entrance reach. As the channel width become smaller the

path shifts toward the channel middle, which is coincident with that for Year 1993. After the two channels joining together, the thalweg paths with a similar spatial distribution were pushed toward the right bank due to confluence flow dynamics.

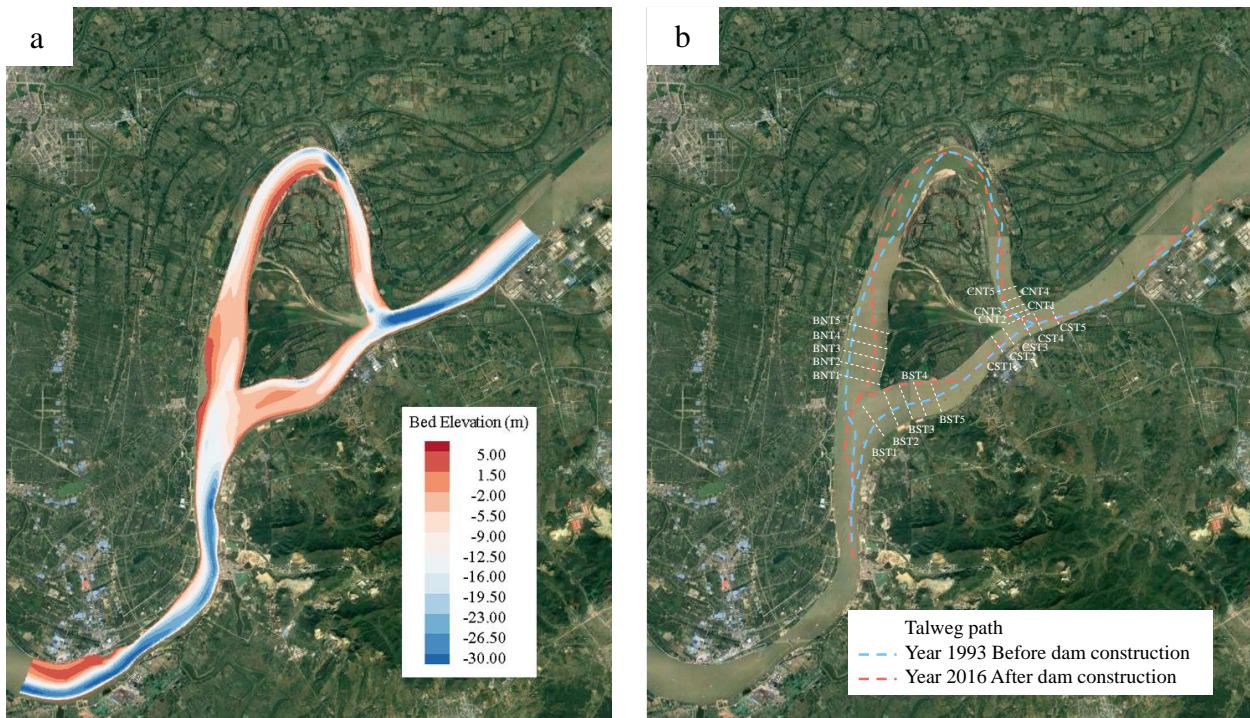


Figure 2 Spatial bed morphology characteristics characterized by (a) bed elevation and (b) thalweg path. Bifurcation angle is  $\sim 60^\circ$ .

To understand the hydrodynamics and morphodynamics at the bifurcation and confluence, it is necessary to extract particular cross sections (see Figure 2b) to present the detailed transverse characteristics of bed morphology (Figure 3). In consistence, the origin is set at the left bank (end) for all cross sections. Overall, it can be interestingly noted that both sub-channels are characterized by a growing channel width when approaching the entrance of both the bifurcation and confluence. For the north channel near the bifurcation entrance (BNT1-BNT2), it is noted that the lowest bed elevation occurs very closed to the right bank, forming a steep transverse slope on the right side and a mild transverse slope on the left side. Therefore, it is anticipated that some bed area on the left

side might be exposed from the water surface under a low water level, particularly when upstream water storage is needed for electricity production in wet season. Along the north channel, the lowest location is gradually elevated and shifts toward the left side and a flat transverse bed profile results. This trend is consistent with the variation of thalweg path for Year 2016 and is mainly attributed to the formation of a high-elevation riffle (see Figure 2a). For the south channel near the bifurcation entrance, the bed topography, starting with a relatively flat bed profile (BST1), is gradually characterized by an ascending tendency in the middle and a scouring tendency on the both sides near the bank (BST2-BST5), which is consistent with the riffle (plugbar) formation (see Figure 2a). Clearly, the scouring effect on the left side is more pronounced than that on the right side, also indicated by the thalweg path (see Figure 2b).

At the confluence (Figure 3b), a sharp bed cutting can be observed in the region closed to the right bank in the north channel. When approaching the confluent site, the bed is further scoured, indicated by the decreasing elevation. The scouring area continuously grows in the transverse direction with the lowest point shifting toward the right side. This effect is because when flow in the north channel joins the south channel, upwelling flows occur resulting in further bed erosion (Biron et al., 1996). In regard to the south channel, the lowest bed elevation location tends to shift toward the right bank at upstream of the confluence (CST1-CST2). However, at the confluent site (CST3), the bed topography suddenly is characterized by a general lower elevation with the lowest point occurring on the left side. After the confluence (CST4-CST5), the cross-section can be observed to be further enlarged due to flow confluence with the lowest elevation shifting toward the right side again.

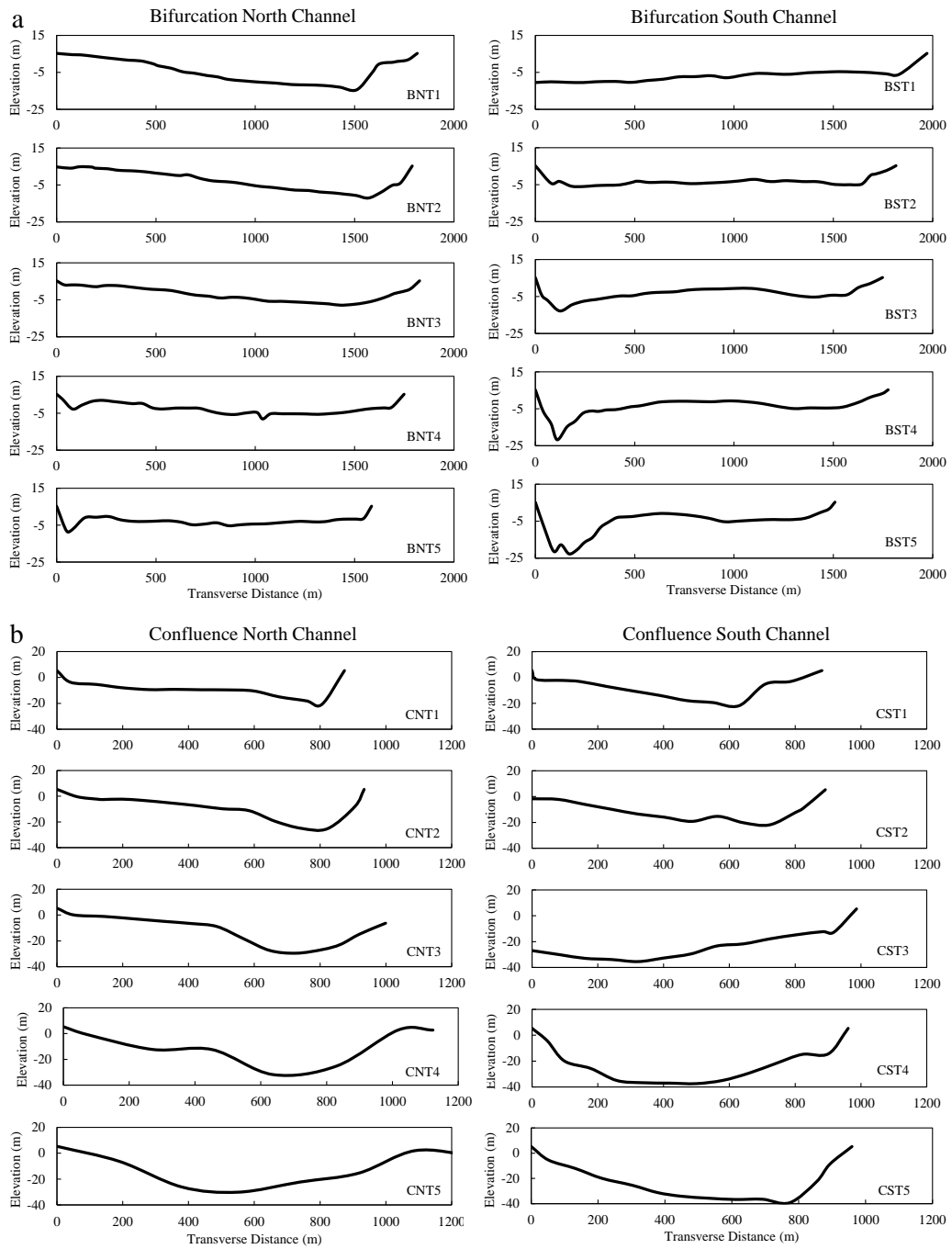


Figure 3 Transverse variation of bed morphology at (a) bifurcation and (b) confluence

## **3.2 Hydrodynamics characteristics simulated by depth-averaged model**

### **3.2.1 Model performance**

Before employing the depth-averaged hydrodynamic model to investigate the hydrodynamics characteristics, the flow velocity data from the field survey is used to validate the hydrodynamic model. To account for the accurate generality of the model, velocities at six cross-sections (see Figure 1b, CS1-CS6) in different regions measured by ADCP from a field survey are used in validation. It is clear that the simulated results of the hydrodynamic model are in a good agreement with the measured results. The errors in regard to all computed velocities are within 10%, indicating the good ability of the hydrodynamic model in modeling large-scale flow motions. Relatively large errors occur in the regions near the inlet (CS1) and bifurcation (CS3 and CS5), where should be characterized by a complex flow field. For example, the simulation near the bifurcation entrance overall underestimates the velocity magnitude of the left part for CS3 located in the north channel; the simulation slightly overestimates the velocity magnitude near the left bank for CS5 located in the south channel. However, it is shown that the model has a good performance in describing the significant effect of flow mixing at the confluence (CS6).

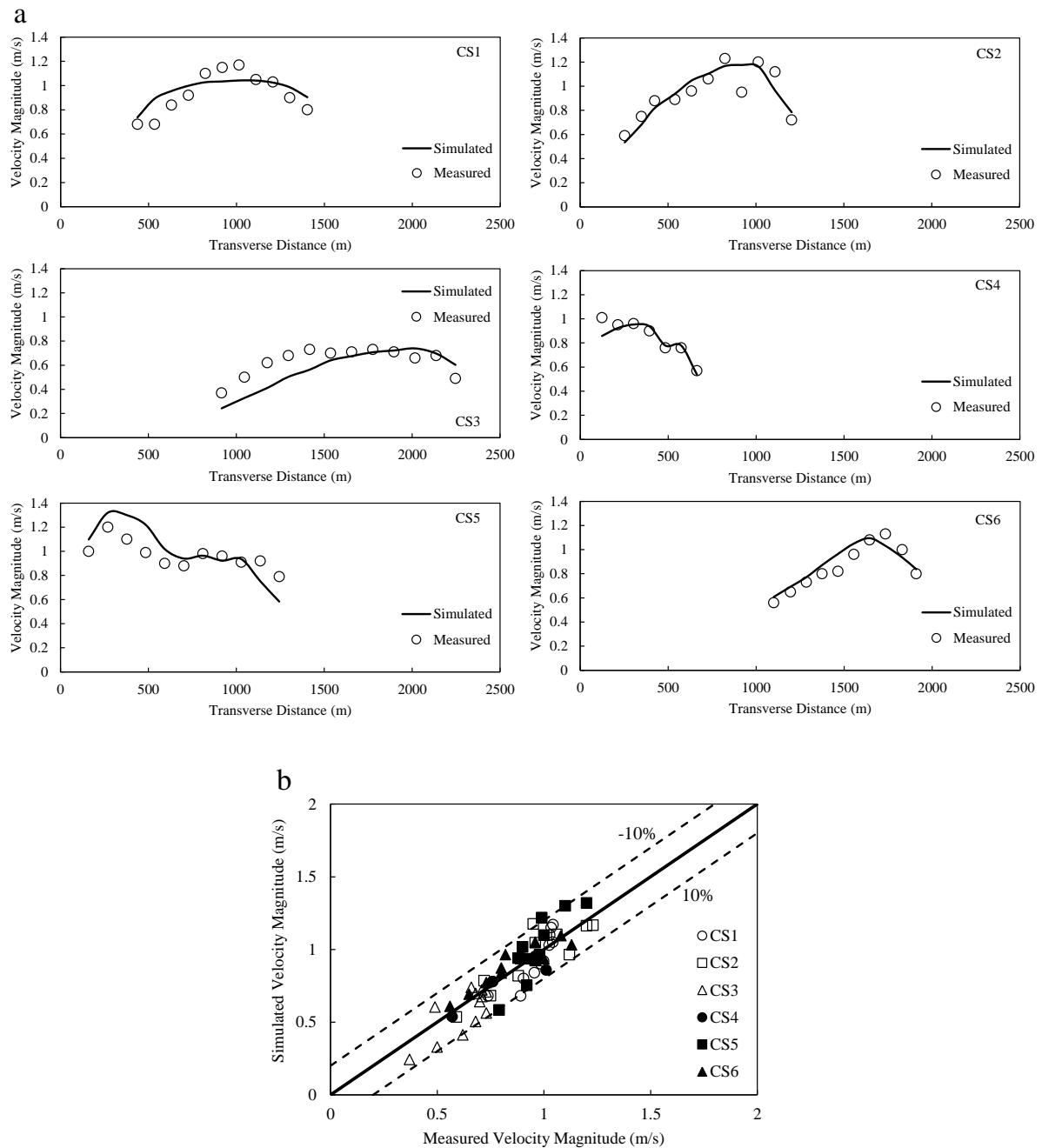


Figure 4 Comparison of velocity magnitude between the measurement and simulation.

### 3.2.2 Hydrodynamics characteristics investigation

In accordance with the survey history, the river morphology is quite stable because of the largely reduced upstream sediment supply after the construction of the TGD and channel regulations by human activities. Therefore, it is reasonable to consider a stable river geometric morphology with

varying flow configurations in a short duration in the computation. A flow-stage relation at the downstream reach was previously derived from the daily record of downstream water discharges and water elevations,

$$z_d = -0.235 \frac{Q^2}{10000} + 3.469 \frac{Q}{10000} - 1.85 \quad (1)$$

Therefore, nine possible flow events of different water discharges and water levels can be formulated to set as boundary conditions. This is able to provide an investigation of hydrodynamics in a field-scale bifurcation-confluence complex in different flow configurations. Table 1 summarizes hydraulic parameters of the flow configurations for nine runs. Particularly, Run 7 has been used to evaluate the validity and performance of the model. The water discharge ranges from 3000-35000 m<sup>3</sup>/s and the downstream outlet water level ranges from -0.78-7.46 m, indicating a range from a low flow level to a high flow level.

Table 1 Summary of flow configurations

	$Q$ (m <sup>3</sup> /s)	$z_d$ (m)	$S$ (m <sup>2</sup> )	$R$ (m)	$U_m$ (m/s)	Fr	Re
Run1	3000	-0.78	2.1×10 <sup>4</sup>	14.5	0.14	0.012	2.1×10 <sup>6</sup>
Run2	5000	-0.12	2.2×10 <sup>4</sup>	15.1	0.23	0.019	3.5×10 <sup>6</sup>
Run3	7000	0.51	2.3×10 <sup>4</sup>	15.7	0.31	0.025	4.9×10 <sup>6</sup>
Run4	11200	1.79	2.4×10 <sup>4</sup>	17.0	0.46	0.036	7.8×10 <sup>6</sup>
Run5	16240	3.21	2.6×10 <sup>4</sup>	18.4	0.62	0.046	1.1×10 <sup>7</sup>
Run6	20000	4.20	2.8×10 <sup>4</sup>	19.3	0.72	0.052	1.4×10 <sup>7</sup>
Run7	24500	5.29	2.9×10 <sup>4</sup>	20.4	0.84	0.059	1.7×10 <sup>7</sup>
Run8	30000	6.49	3.1×10 <sup>4</sup>	21.6	0.97	0.067	2.1×10 <sup>7</sup>
Run9	35000	7.46	3.2×10 <sup>4</sup>	22.5	1.08	0.073	2.4×10 <sup>7</sup>

The above statistics account for the outlet boundary condition for current simulation.  $Q$  = water discharge,  $z_d$  = water level,  $S$  = cross-sectional area,  $H$  = water depth,  $R$  = hydraulic radius,  $U_m$  = mean velocity,  $Fr = U_m / \sqrt{gH}$  = Froude number,  $Re = U_m R / \nu$  = Reynolds number,  $g = 9.81 \text{ m/s}^2$  = gravitational acceleration and  $\nu = 1.01 \times 10^{-6} \text{ m}^2/\text{s}$  = kinematic viscosity.

## Discharge distribution

By integrating depth-averaged velocities with the channel width at the entrance cross-section of each sub-channel, water discharges due to flow bifurcation can be calculated. As shown in Figure 7, the north channel discharge is positively linearly related to the south channel discharge. The discharge ratio is nearly constant maintained as  $\sim 1.65$ . Figure 8 compares the recent 10-year monitoring data with the simulated results, it is found that the model has a good performance in simulating water discharge distributed into the two sub-channels with a varying net water discharge (water level).

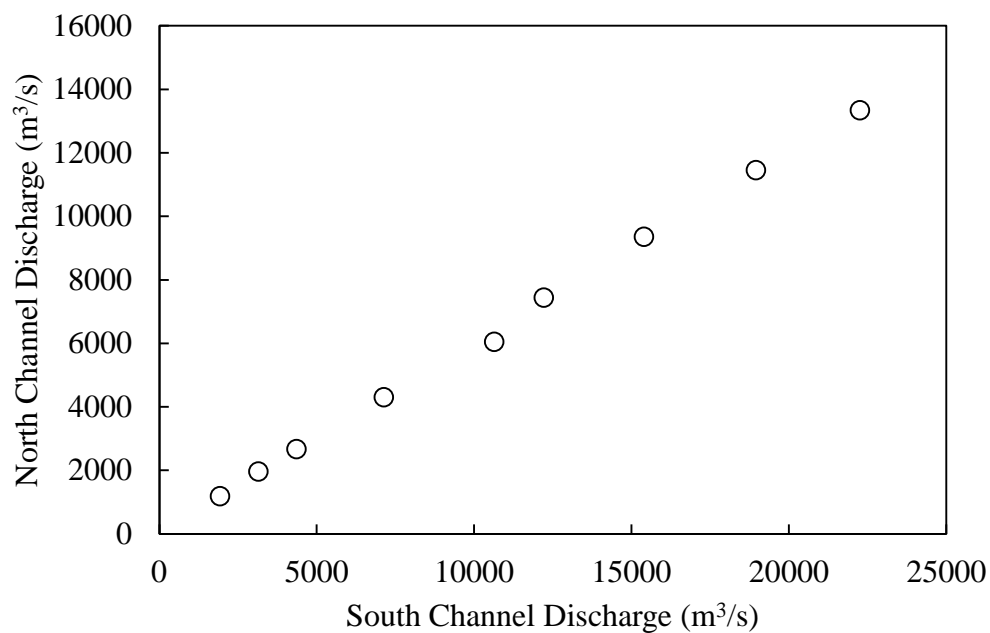


Figure 7 Discharge partitioning by the bifurcation at different water levels.

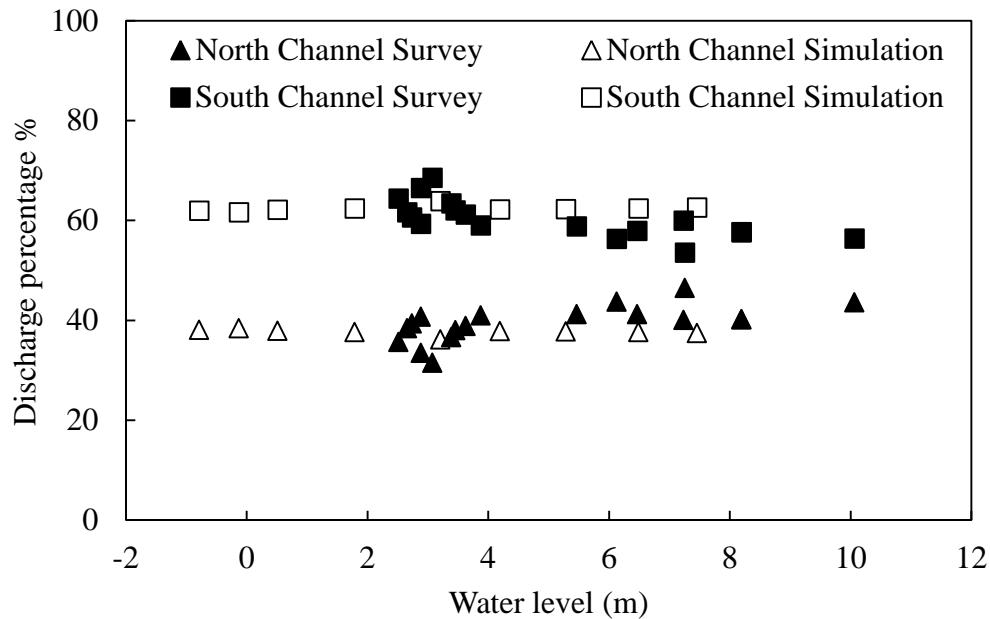
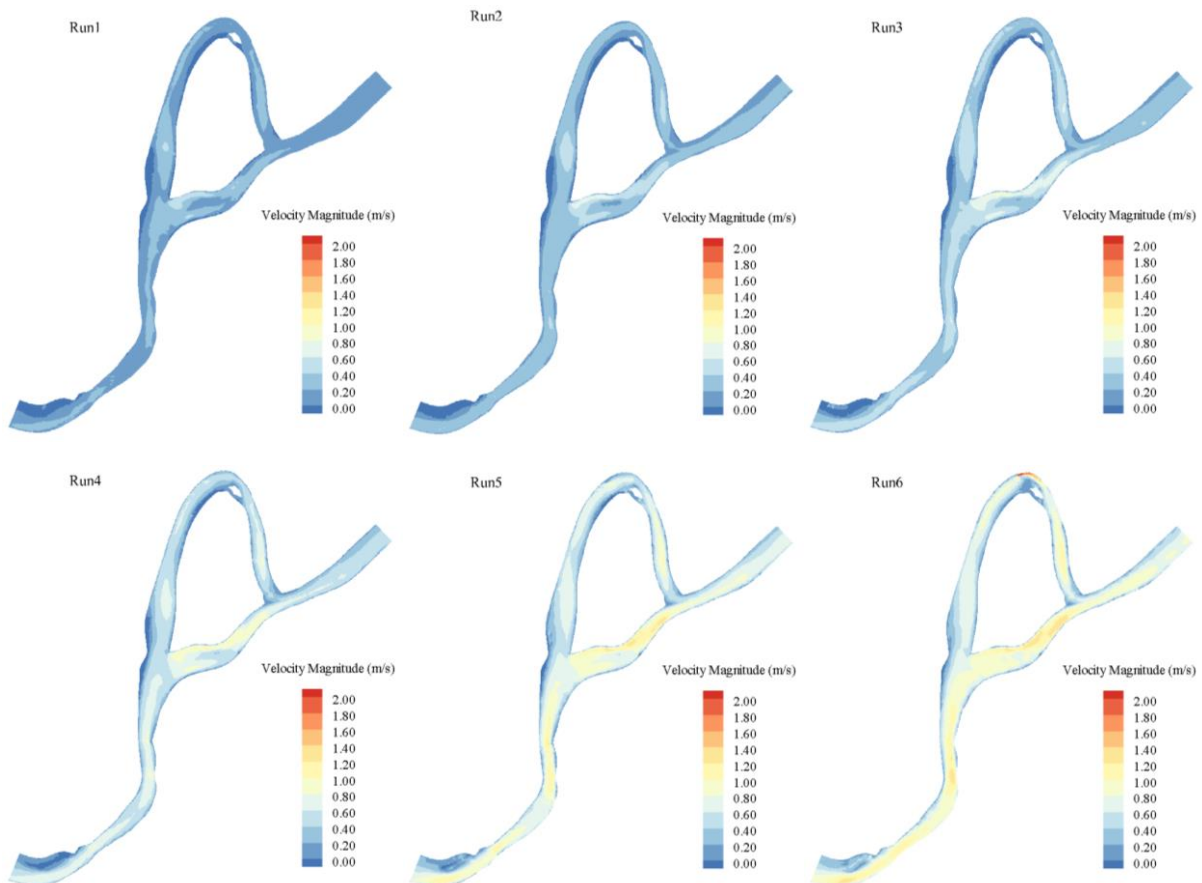


Figure 8 Discharge percentage as a function of water level.

### Hydrodynamics characteristics map

Figure 9 shows the spatial distribution of velocity magnitude ( $U_t$ ), which is the vector summation of velocities ( $U$  and  $V$ ) in the  $x$  direction and  $y$  direction. For runs with low water discharges (e.g., Run1-Run4), zero velocity can be found in the regions of inner bank of the upstream meander, right bank of the north channel near the bifurcation entrance and right bank of the upstream limb of the bar-induced bend in the north channel. These regions are responsible for the high bed elevation. Clearly, it can be noted that high velocity regions occur in different areas of the entire reach. At the downstream limb of the meander, high velocity is distributed along the side of outer banks for runs of small water discharges. As the water discharge increases, the high velocity core gradually concentrates the narrowest section downstream the bend apex. This is because with the increase in water level increases river can use the point bar near the bend apex to convey waters so that the increase in flow velocity insignificant. Therefore, topographic steering plays a significant role in redistribution of flow mass. At a low water level (e.g. Run1-Run3), high velocity also appears in

regions near the bifurcation in both sub-channels, where the bed morphology is characterized by a high elevation normally referred to as riffles. In contrast, a high water level leads the high velocity regions near the bifurcation to the downstream reach of the two sub-channels. It should be noted that a significant increase in velocity occurs in the south channel near the confluence, where corresponds to a decrease in bed elevation and a decrease in channel width. After two sub-channels join at the confluence, velocity overall decreases with relative high velocity appearing on the opposite side of the confluent interface. Meanwhile, a low velocity zone always exists at the upstream corner of the confluence interface under different flow conditions. At the downstream comer of the confluence interface, a low velocity zone occurs only for small water discharges (Run1-Run6) and gradually disappears as water discharge increases (Run7-Run9). This is associated with the evolution of flow separation at the confluence with non-flat bed topography.



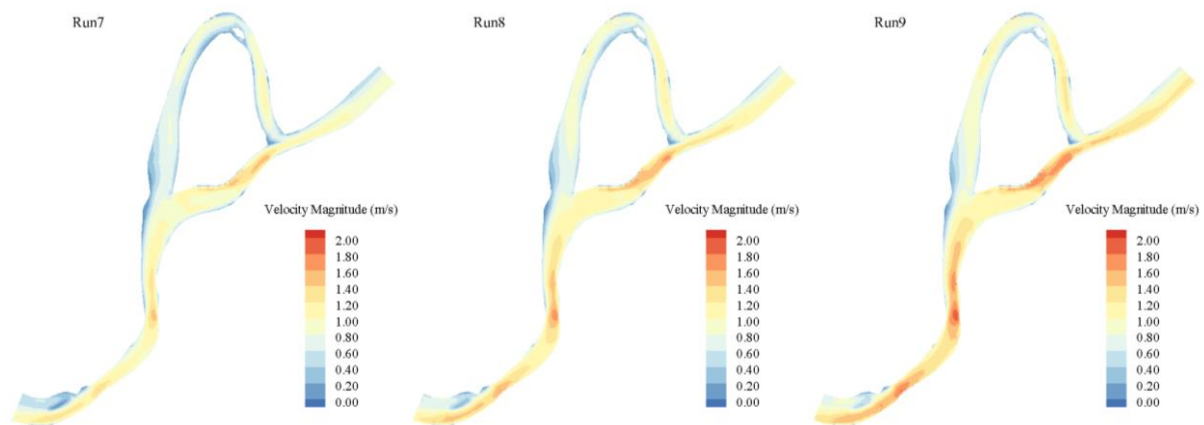


Figure 9 Magnitude of depth-averaged velocity under different flow configurations

Surely, the spatial distribution of velocity can partially reflect how the river center bar redistributes flow mass. However, this reflection is untrue under sharply varying bed topography such as pools, riffles and sediment bars. For example, when a high velocity exists over a shallow water depth, the unit mass flux is possibly small compared to other deep region. Herein, the product of depth-averaged velocity ( $U_i$ ) and water depth ( $h$ ) is used to indicate the unit flow mass flux, ( $\text{Flux}=U_i h$ ). Figure 10 shows the spatial distribution of mass flux over the entire reach. Similar to the velocity magnitude, the mass flux at the reach of the upstream meander has a high value on the side of the outer bank due to the topographic steering of the bend and point bar, and the effect reaches out the region until the bifurcation. Along the side of the inner bank, the mass flux, however, is relatively small. Different from the distribution of velocity magnitude, the mass flux always stays low around the bifurcation even under small water discharges. In contrast, the velocity magnitude around the bifurcation is high (Run1-Run3, Figure 9). This is attributed to the shallow water depth over the riffle topography at the bifurcation. For the north channel, an elongated high mass flux belt is formed near the outer bank around the bar-induced bend. Furthermore, this flux belt expands upstream and downstream, and is widened as the water discharge increases. For the south channel, the mass flux of relatively high value appears near the bar side first and then shifts to the opposite at

downstream. This distribution pattern is consistent with the velocity magnitude. When the two sub-channels join at the confluence, a high mass flux zone occurs at the pool region. Although the velocity in the pool region is not high over the entire reach, a large water depth plays a significant role in contributing the mass flux.

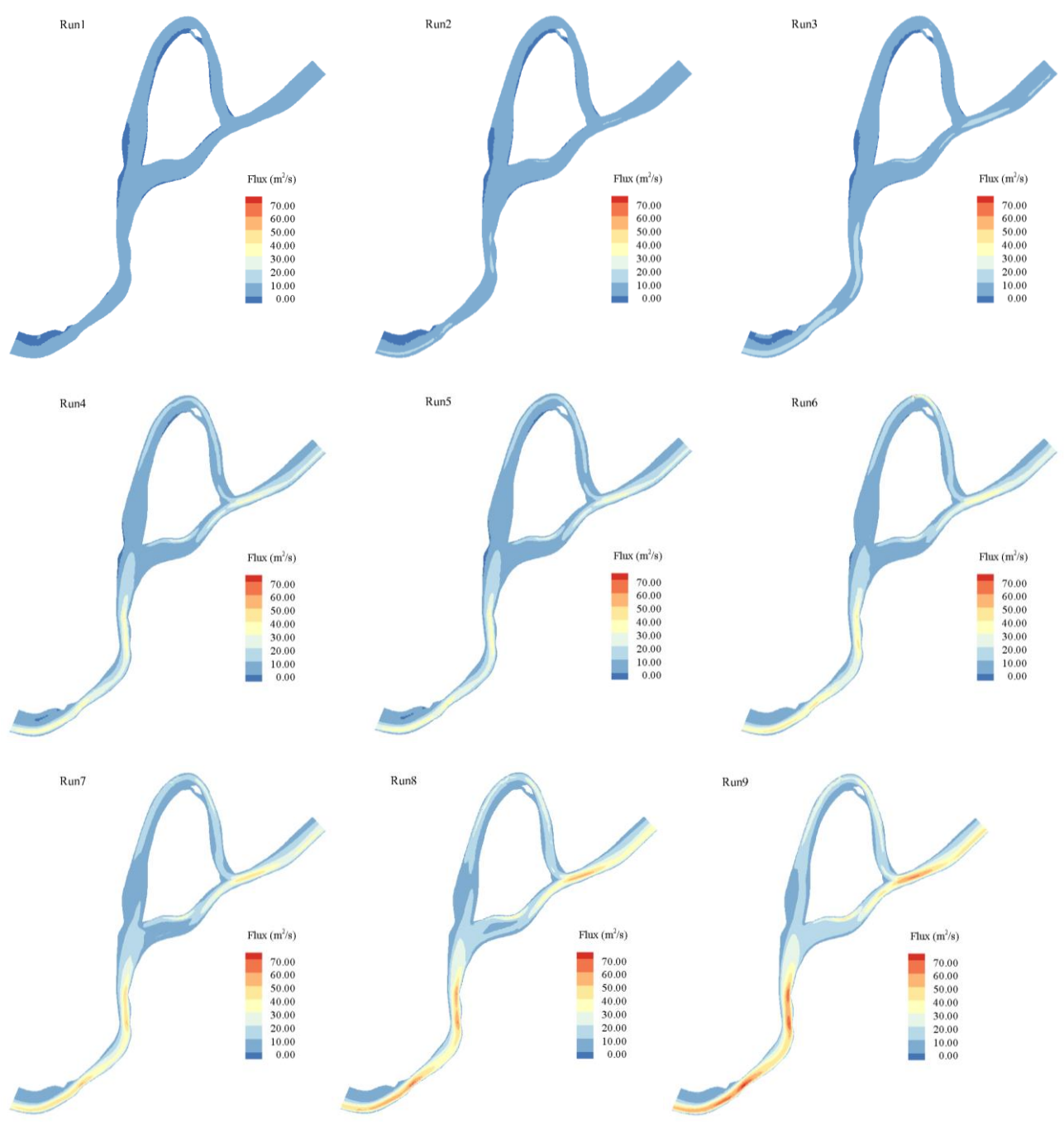
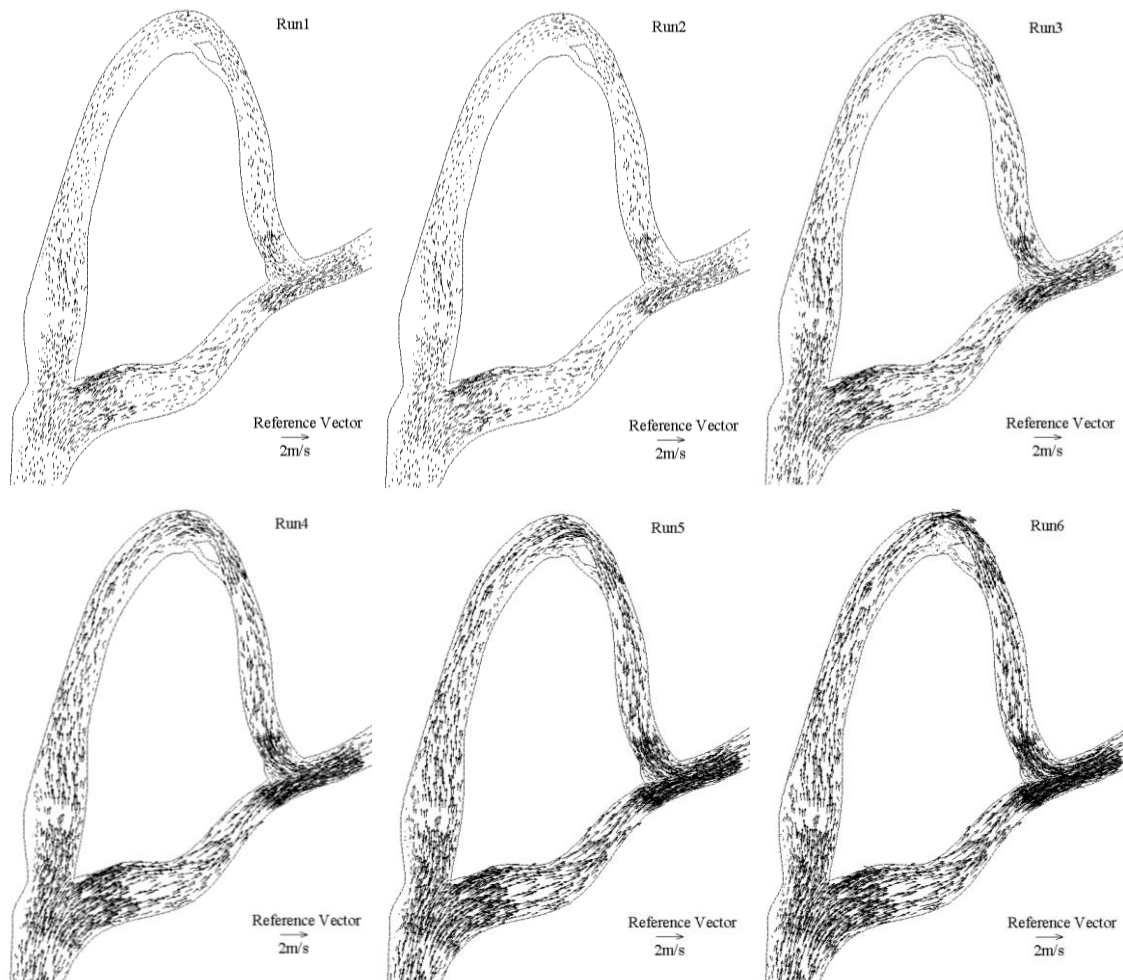


Figure 10 Depth-integrated flux (water discharge) under different flow configurations

With the recognition of flow mass redistribution characteristics over the bed morphology,  $U$ - $V$  vectors are illustrated in Figure 11 to understand how the river center bar and its impacted bed topography influences flow motions in the longitudinal ( $x$ -) and transverse ( $y$ -) directions. This can provide more insights into the understanding of bifurcation-confluence hydrodynamics, sediment dynamics and morphodynamics under different flow configurations. Herein, only flow fields around the river center bar are given since numerous studies about flow fields over a meander can be existent (Kleinhans et al., 2006; Van Denderen et al., 2018). Under a low flow, the north channel is situated in a non-bankful state since sediment bar of more area can be found. The topographic steering of flow by those sediment bars can be observed in the north channel near the bifurcation entrance and the inner bank of the bar-induced bend. Although the south channel is always situated in a bankful state, flow velocity with a significant transverse component occurs at the channel center, where a riffle is located. As the water discharge increases, flow occupies the entire cross-section and leads the entire reach to being in a bankful state under a high flow. At this moment, the topographic steering of flow due to the bed elevation variation becomes insignificant, and velocity vectors are mainly dominated by the channel bank geometry such as the varying channel width, curved channel banks and confluent channels. For example, flow divergence and convergence appear as the channel width varies near the bifurcation entrance. Along the bend in the north channel, flow velocity vectors mainly follow the streamwise direction, not forming flow circulation near the inner bank of the downstream limb under varying flow configurations.

Figure 12 also shows that velocity vectors at confluence evolve with the varying water discharges. Under a low water discharge, the velocity vectors mainly concentrate on the left side of the bed, where a pool region exists. This requires a long path before the two channels confluence. As a result,

flow separation forms on the opposite side. As water discharge increases, velocity vectors on the right side of bed become significant, which leads to the re-disappearance of the flow separation. A detailed description of the confluence velocity vectors is illustrated in Figure XX. In this study, the hydrodynamics in the confluence is particularly paid attention. Under a low flow, a flow circulation and a stagnation zone can be observed near the downstream point and upstream point of the confluence interface, respectively. However, the geometric size of the flow circulation gradually decays and even diminishes as the water discharge continuously increases, so does the stagnation zone.



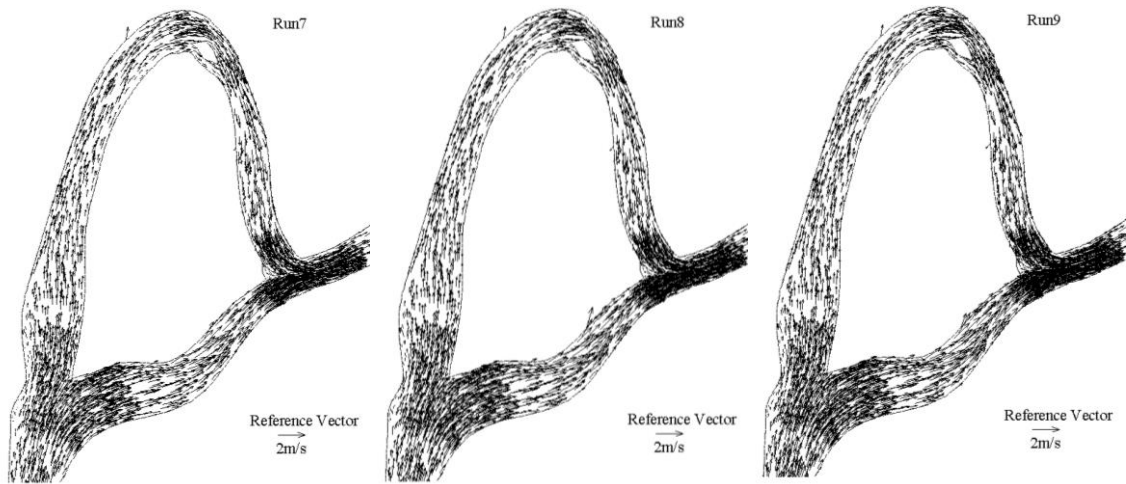


Figure11 Velocity vectors ( $U-V$ ) around the river bar under different flow configurations

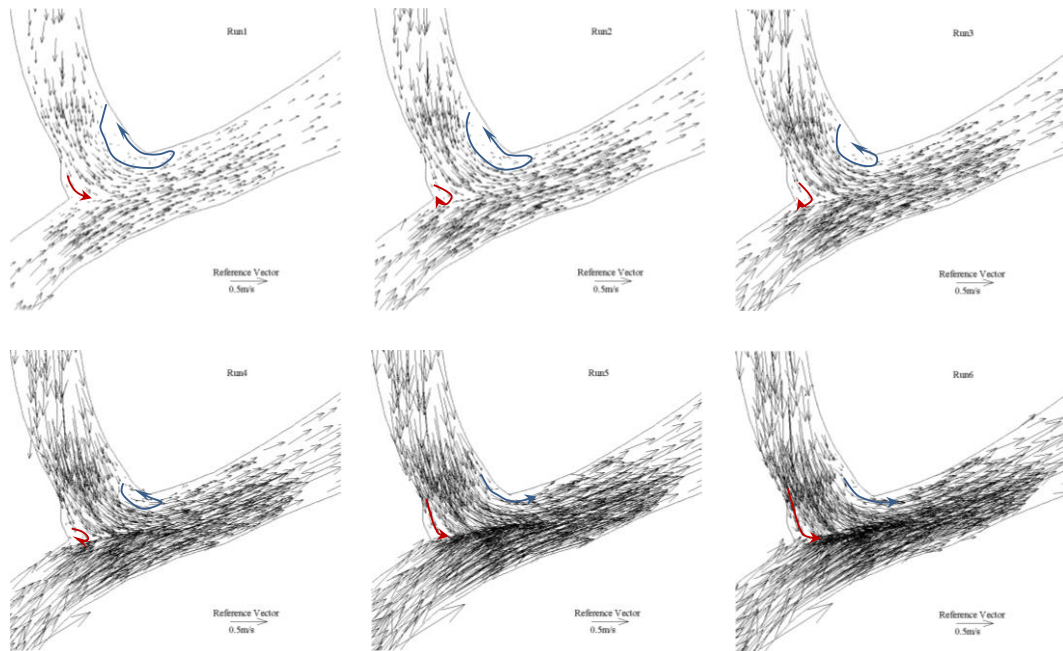
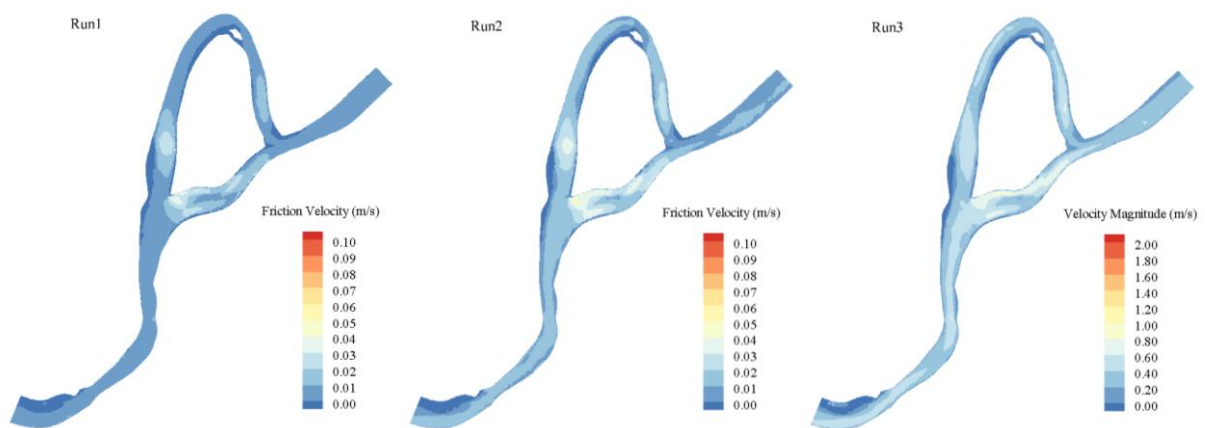


Figure 12 Characteristics of flow separation and stagnation at the confluence under different flow configurations

Figure 13 shows the spatial distribution of bed friction velocity, which can indicate the potential of sediment motion and morphological evolution. In the simulation, the bed friction coefficient is a function of a constant Manning roughness coefficient and water depth. Then, the friction velocity is derived from the net velocity and bed friction coefficient. It should be noted that the friction velocity is negatively related to local water depth and positively related to velocity magnitude.

When water discharge is small (Run1-Run3), maximum values of bed friction velocity occur in the entrance of both the two sub-channels with relatively high bed elevation and low water depth, which is similar to the distribution of the velocity magnitude. As water discharge (or water level) increases, the high friction velocity shifts the downstream reach of the south channel ahead of the confluence with a decreasing bed elevation compared with the upstream reach. For the north channel, the high-value region also shifts to the downstream reach of the south channel. It is clearly noted that under a high flow (Run7-Run9), the friction velocity in the south channel is overall larger than that in the north channel. Interestingly, as water discharge (water level) continuously increases, a friction velocity belt of overall high value starting at the outer bed side of the upstream meander forms, all way expands over the entire south channel. The high-value belt finally extends to the confluence (Run8-Run9), mainly distributed on the opposite side of the confluence interface, where an elongated pool is formed.



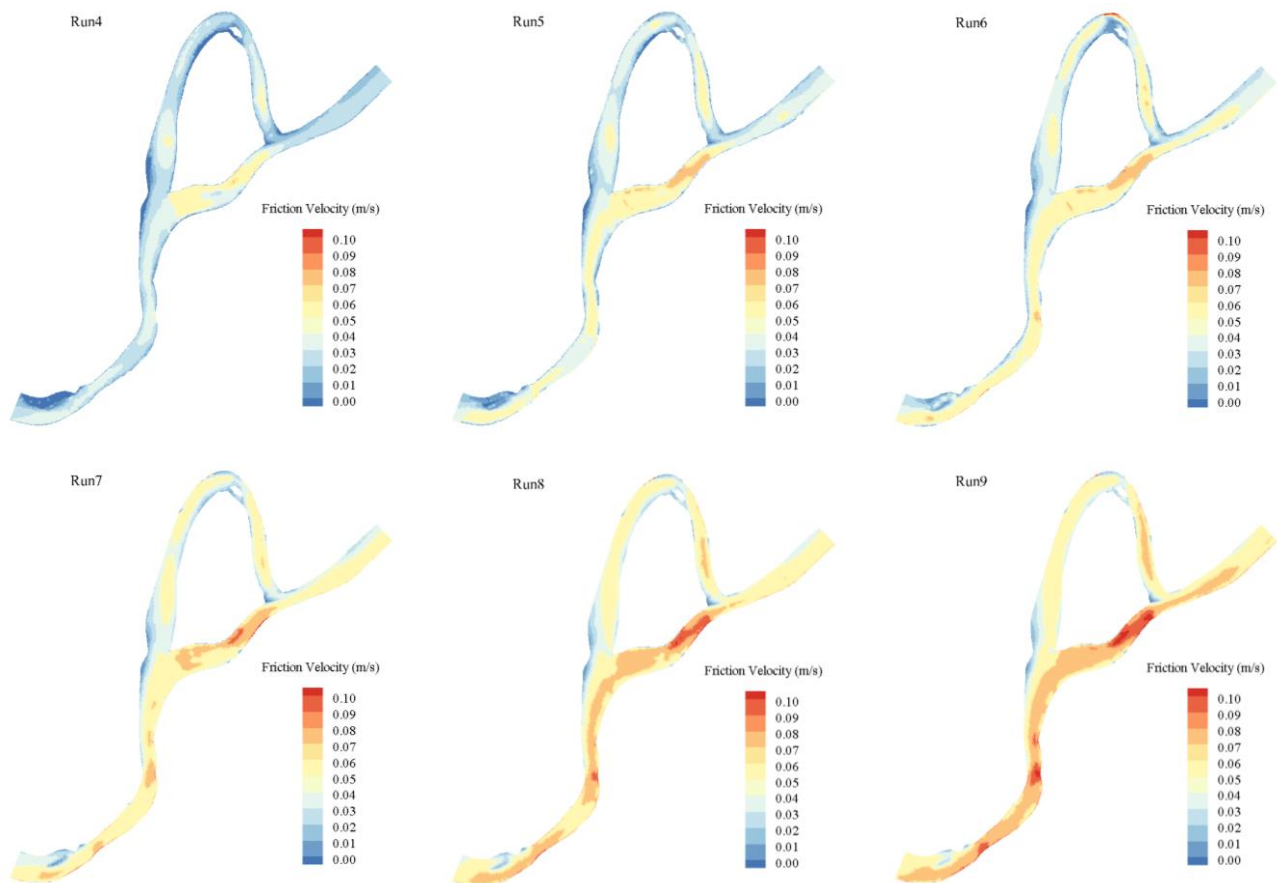


Figure 13 Friction velocity under different flow configurations.

## 4 Discussion

As commonly observed in the natural rivers (Kleinhans et al., 2008; Van Denderen et al., 2018; Zinger et al., 2013), a meander occurs at upstream before the main stem is bifurcated into two sub-channels. Therefore, flow and sediment dynamics need to be readjusted before entering the bifurcation channel system (Kleinhans et al., 2008). Unlike other field studies with a large bifurcation angle (Constantine et al., 2010; Kleinhans et al., 2013; Zinger et al., 2013), the two bifurcated sub-channels are still characterized by entrance riffles (plugbars). However, the plugbar for the south channel is closer to the channel entrance relative to the north channel. The cause might be the south channel has a very large turning angle in regard to the upstream reach, while the north

channel is nearly the extension of the upstream reach. As demonstrated by (Constantine et al., 2010) and (Van Denderen et al., 2018), the sub-channel with a large bifurcation angle tends to enable sediment deposition at the entrance. Interestingly, outer bank sediment bar only occurs in the north channel. This is contrary to previous findings that sediment bars commonly occur along the outer bank of sub-channels with a large bifurcation angle, which are favored by flow separations leading to sediment deposition (Constantine et al., 2010; Dutta et al., 2017). The north channel has a length  $\sim 3$  times of the south channel, indicating that the corresponding reach-averaged bed slope of the north channel is  $\sim 1/3$  of the south channel. This might significantly influence overall sediment transport capacity and bed morphology pattern of the two sub-channels.

Near the confluence, the sediment bars and pool have particular alignments, which are different from previous field studies. The pool with an elongated shape is initially developed in the region two tributaries join together across nearly the entire cross section of downstream the confluence. This leaves no space for sediment depositing downstream of the inner bank of the confluence, which is observed in other studies (Best, 1988; Biron et al., 1996; Rhoads and Kenworthy, 1995; Szupiany et al., 2009; Zinger et al., 2013). However, a sediment bar is formed in an upstream tributary (north channel) just ahead of the confluence, coincident with the flow separation under low flows as illustrated by simulated results (Figure 12). The sediment bar seems to be a result of the combining effect of the upstream tributary sinuosity and the flow confluence. But this unusual phenomenon needs to be explored using laboratory flumes or more field data.

This study assumes a stable bank and bed morphology in a short term after the dam construction and channel regulation by human activities. This study mainly focuses on the hydrodynamics as a result of the river morphology and the varying flow configurations; thus, sediment motion and bed

morphological change are not considered herein. Different flow-stage combinations in a range from low flow to high flow were adopted into a depth-averaged hydrodynamic model to investigate flow characteristics over the known bed morphology. A good agreement between the field survey of velocity and the simulation demonstrate the good performance of the model in simulating complex flows (e.g. flows in meander, bifurcation and confluence) in a large-scale river reach. This fact is consistent with other reports which applied the hydrodynamic model to compute other large-scale river cases (Nelson et al., 2016; Nones et al., 2018).

The simulated results show that with a varying flow configuration, the discharge redistribution because of the bifurcation is relatively stable, which is fairly consistent with a 10-year field monitoring (Figure 8). The discharge ratio of the south channel to north channel is maintained to be  $\sim 1.65$  (Figure 7), indicating that the south channel functions as the main channel to convey the larger discharge. However, this is not consistent with previous findings, which indicate that the discharge ratio of sub-channels tends to approach unity as water discharge increases (Hackney et al., 2018; Szupiany et al., 2012).

High velocity regions occur in different locations and shift spatially when a low flow transforms into a high flow. Under a low flow, high velocity is found to occur in riffle regions near the bifurcation entrance and velocity in pool regions at the meander, however, is relatively small. As the water discharge increases, velocity in the entire reach increases. However, the pool regions have a more rapid increase in velocity than the riffle regions and high velocity occurs in pool regions instead. This phenomenon is consistent with the previous finding referred to as velocity reversal in pool-riffle sequences when flow varies between low level and high level (Keller and Florsheim, 1993; MacWilliams Jr et al., 2006; Thompson, 2011). In fact, the spatial distribution of velocity

cannot reflect the true flow mass distribution. By calculation, high flow mass flux always occurs in pool regions, for example, at the meander and confluence, which is also similar with previous findings (Blanckaert, 2010; Konsoer et al., 2016). This is because apart from the contribution of velocity, the bed topography plays a more significant role in the contribution. Riffles occurring around the bifurcation having large channel widths are characterized by low flow mass fluxes. However, by integration over the channel width, the total water discharge still remains a high level. Varying from low flows to high flows, the velocity vector fields also vary as illustrated by the simulated results. The bed topography variation, under a low flow, plays a dominant role in directing flow in the river. High-elevation bed region such as sediment bars can protrude from the water surface. Topographic steering of flow by those high bed forms causes more transverse motions of flows in bifurcation regions. Even if some shallows (riffles or plugbars) near the entrance of the sub-channels are submerged by water surface, transverse flow motions driven by transverse bed gradients still exist. Under a high flow, the entire reach is situated at a bankful state. The channel uses sediment bars to convey waters, which reduces impact of transverse variations of bed the topography. Therefore, the effect of flow steering due to bankline variation becomes more profound. With respect to the simulated flow configurations, flow separations are diminished or even do not develop in regions with channel widths expanding or banklines bending. The cause might be attributed to that the boundary variation is not enough to trigger the formation of reversed flow (Zinger et al., 2013) . Flow separation also does not occur at the downstream reach of the bar-induced bend apex when flow ranges from a low discharge to high discharge. This is not consistent with previous observations (Blanckaert, 2010; Thorne et al., 1985).

A flow separation zone occurs at the downstream inner bank of the confluence under low flows

(Figure 13). The flow separation completely disappears when water discharge continuously increases. In existing studies, a confluence might and might not have flow separation zone (Biron et al., 1996; Rhoads and Kenworthy, 1995; Szupiany et al., 2009; Zinger et al., 2013) and its existence might be attributed to the characteristics of topographically-steered flows at the confluence as addressed by (Best, 1988; Szupiany et al., 2009). Interestingly, different from some previous findings that the flow separation zone is aligned along the main channel downstream the confluence (Rhoads and Kenworthy, 1995; Yang et al., 2009; Zinger et al., 2013), the flow separation zone initially is developed at the upstream tributary (the north channel) and expands to the downstream main channel. Another stagnation zone characterized by flow circulation appears at the upstream corner of the confluence when water discharge is small. This hydrodynamic phenomenon also disappears under high flows, similar to the behavior of downstream corner flow separation.

Finally, the results demonstrate that similar to the distribution of velocity, riffle regions near the bifurcation are found to be with higher bed friction velocity. As flow is transformed to a high level, the high friction velocity zone shifts to pool regions, while the friction velocity in riffle regions still remains high value. This is also consistent with the velocity-reversal phenomenon in a pool-riffle sequence. It is very clearly noted that the south channel is linked to the upstream main channel by a friction velocity belt of similar and high friction velocity. This suggests that the north channel is characterized with more sediment deposition, which is, however, less favored by the south channel. The potential of sediment motion corresponds to the large water conveyance ability of the south channel. The opposite tendencies of water and sediment transport in a bifurcated channel system are substantially related to hydrodynamics and sediment dynamics in the upstream meander, explained

by Kleinhans et al. (2006), Kleinhans et al. (2008) and Van Denderen et al. (2018). This trend has been confirmed by a long-term site monitoring after the construction of the TGD.

## 5 Conclusion

This paper presents a study of morphological characteristics of a large-scale bifurcation-confluence complex formed by a river center bar after the establishment of TGD in the Yangtze River, China. The detailed field survey and numerical modeling have been conducted for this investigation. The main results and findings of this study can be summarized as follows.

(1) Similar to other field observations, a meander exists before the main stem is bifurcated into two sub-channels. The length of the North sub-channel approaches around 3 times of that of the South channel with a large bifurcation angle, indicating a small bed slope of the North channel and thus the nature of sediment deposition. With regard to the North channel, a secondary meander in the study reach is formed due to the morphology of the river center bar. Meanwhile, the South channel nearly maintaining its orientation is rejoined by the North channel with a nearly perpendicular confluence angle;

(2) Significantly impacted by the complex bankline geometry, as well as hydrodynamics and sediment dynamics, the bed morphology is characterized by various typical bed forms such as pools, riffles and sediment bars. In general, the outer bank of meander reaches is coincident with deep pools and the inner bank is coincident with shallow sediment bars. Near the bifurcation entrance, riffles or plugbars are formed in the two bifurcated channels. The shallow bed topography for the South channel, however, is closer to the entrance, indicating the function of the large bifurcation angle. At the confluence, an elongated pool across the entire cross-section is formed, being aligned

along the rejoined main stem. However, a sediment bar shifts upward the North channel, which is different from common scenarios that sediment bar occurs right downstream the confluence corner in the main stem;

(3) A good agreement between the simulated results and measured results, over the known bed morphology, indicates acceptable accuracy and validity of the used hydrodynamic model in simulating complicated flows in a large-scale bifurcation-confluence complex. After validation, the numerical model is applied for the nine sets of flow stages, varying from a low flow to a high flow, to investigate the evolution of the hydrodynamics over the unchanged bed boundary. The application results show that the discharge ratio of the South channel to North channel is maintained to be about 1.65 as water discharge (level) continuously increases. In fact, this trend is consistent with a 10-year monitoring after the construction of the TGD;

(4) As flow varies from low levels to high levels, the river bank and bed morphology may have significant impact on the spatial distribution of flow velocity and flow mass flux. Specifically, under low flow conditions, high velocity may occur in riffle (plugbar) regions near the bifurcation entrance and also in pool regions at the primary meander. However, high velocity regions could have shifted to the pool regions. The spatial evolution of flow velocity under varying flows, referred to as velocity-reversal phenomenon, can be found in mesoscale pool-riffle sequences. In contrast, high flow mass flux only occurs in pool regions at the primary meander and confluence, which may be attributed to the substantial contribution of the water depth;

(5) The visualized numerical results of velocity vector fields under varying flows suggest that, under a low flow, the effect of topographic-steering of flow by shallow bed topography such as sediment bars and riffles (plugbars) could have a dominant role in determining the local direction of

flow motion. Under high flows, however, the effect of flow steering due to bankline variation becomes more profound, thereby greatly influences the flow motion. For the confluence hydrodynamics, flow separation occurs under low flows only, and its size is diminished when water discharge (level) increases. The location of flow separation is coincident with the sediment bar at the upstream tributary (North channel). This is due to the fact that confluence sediment bar is commonly accompanied by flow separation. Meanwhile, flow stagnation also occurs at the upstream corner of the confluence under low flows only and it disappears under high flows.

(6) Finally, the spatial distribution of bed friction velocity is illustrated to indicate potentials of sediment motion and bed morphological evolution. Similar to velocity-reversal phenomenon, friction velocity over shallow beds near the bifurcation is overall greater than deep regions. Under high flow condition, the relatively high friction velocity may shift from the shallow beds to deep beds. Particularly, the highest core occurs at the downstream reach of the South channel ahead of the confluence. Moreover, for a high flow, a clear belt of high friction velocity is observed to link the upstream main stem and the South channel, indicating the favored sediment deposition by the North channel. This result may provide the scientific explanation and support to historical operations of entrance closure of the North channel along the Yangtze river.

## **Reference**

- Best, J.L. (1988). Sediment transport and bed morphology at river channel confluences. *Sedimentology*, 35, 481-498.
- Best, J.L., Reid, I. (1984). Separation zone at open-channel junctions. *Journal of Hydraulic Engineering*, 110, 1588-1594.

- Biron, P., Best, J.L., Roy, A.G. (1996). Effects of bed discordance on flow dynamics at open channel confluences. *Journal of Hydraulic Engineering*, 122, 676-682.
- Blanckaert, K. (2010). Topographic steering, flow recirculation, velocity redistribution, and bed topography in sharp meander bends. *Water Resources Research*, 46.
- Brandt, S.A. (2000). Classification of geomorphological effects downstream of dams. *Catena*, 40, 375-401.
- Constantine, J.A., Dunne, T., Piegay, H., Mathias Kondolf, G. (2010). Controls on the alluviation of oxbow lakes by bed-material load along the Sacramento River, California. *Sedimentology*, 57, 389-407.
- Dutta, S., Wang, D., Tassi, P., Garcia, M.H. (2017). Three-dimensional numerical modeling of the Bulle effect: the nonlinear distribution of near-bed sediment at fluvial diversions. *Earth Surface Processes and Landforms*, 42, 2322-2337.
- Garcia, M., Niño, Y. (1993). Dynamics of sediment bars in straight and meandering channels: experiments on the resonance phenomenon. *Journal of Hydraulic Research*, 31, 739-761.
- Graf, W.L. (2006). Downstream hydrologic and geomorphic effects of large dams on American rivers. *Geomorphology*, 79, 336-360.
- Hackney, C.R., Darby, S.E., Parsons, D.R., Leyland, J., Aalto, R., Nicholas, A.P., Best, J.L. (2018). The influence of flow discharge variations on the morphodynamics of a diffluence–confluence unit on a large river. *Earth Surface Processes and Landforms*, 43, 349-362.

- Hardy, R., Lane, S., Yu, D. (2011). Flow structures at an idealized bifurcation: a numerical experiment. *Earth Surface Processes and Landforms*, 36, 2083-2096.
- Hassan, M.A., Woodsmith, R.D. (2004). Bed load transport in an obstruction-formed pool in a forest, gravelbed stream. *Geomorphology*, 58, 203-221.
- Keller, E., Florsheim, J.L. (1993). Velocity-reversal hypothesis: A model approach. *Earth Surface Processes and Landforms*, 18, 733-740.
- Kleinhans, M., Jagers, B., Mosselman, E., Sloff, K. (2006). Effect of upstream meanders on bifurcation stability and sediment division in 1D, 2D and 3D models. *River Flow 2006*, 1355-1362.
- Kleinhans, M., Jagers, H., Mosselman, E., Sloff, C. (2008). Bifurcation dynamics and avulsion duration in meandering rivers by one-dimensional and three-dimensional models. *Water resources research*, 44.
- Kleinhans, M.G., Ferguson, R.I., Lane, S.N., Hardy, R.J. (2013). Splitting rivers at their seams: bifurcations and avulsion. *Earth Surface Processes and Landforms*, 38, 47-61.
- Konsoer, K.M., Rhoads, B.L., Best, J.L., Langendoen, E.J., Abad, J.D., Dan, R.P., Garcia, M.H. (2016). Three-dimensional flow structure and bed morphology in large elongate meander loops with different outer bank roughness characteristics. *Water Resources Research*, 52, 9621-9641.
- Le, T.B., Khosronejad, A., Sotiropoulos, F., Bartelt, N., Woldeamlak, S., Dewall, P. (2018). Large-eddy simulation of the Mississippi River under base-flow condition: hydrodynamics of a natural diffluence-confluence region. *Journal of Hydraulic Research*, 1-16.

Liu, T.-h., Li, C., Fan, B.-l. (2012). Experimental study on flow pattern and sediment transportation at a 90 open-channel confluence. *International Journal of Sediment Research*, 27, 178-187.

Lomax, H., Pulliam, T.H., Zingg, D.W. (2013). *Fundamentals of computational fluid dynamics*, Springer Science & Business Media.

Lyu, Y., Zheng, S., Tan, G., Shu, C. (2018). Effects of Three Gorges Dam operation on spatial distribution and evolution of channel thalweg in the Yichang-Chenglingji Reach of the Middle Yangtze River, China. *Journal of hydrology*, 565, 429-442.

Ma, Y., Huang, H.Q., Nanson, G.C., Li, Y., Yao, W. (2012). Channel adjustments in response to the operation of large dams: The upper reach of the lower Yellow River. *Geomorphology*, 147, 35-48.

MacWilliams Jr, M.L., Wheaton, J.M., Pasternack, G.B., Street, R.L., Kitanidis, P.K. (2006). Flow convergence routing hypothesis for pool-riffle maintenance in alluvial rivers. *Water Resources Research*, 42.

MFlow\_02 (2018). Solver Manuals, iRIC Software. Available online: <http://i-ric.org>

Nelson, J.M., Shimizu, Y., Abe, T., Asahi, K., Gamou, M., Inoue, T., Iwasaki, T., Kakinuma, T., Kawamura, S., Kimura, I. (2016). The international river interface cooperative: Public domain flow and morphodynamics software for education and applications. *Advances in Water Resources*, 93, 62-74.

Nezu, I., Nakagawa, H. (1993). *Turbulence in open-channel flows*, IAHR monograph series. AA Balkema, Rotterdam, 1-281.

Niu, C., Jia, D., Zhang, X. (2017). Riverbed evolution and navigation obstructing characteristics at Heishazhou Southern Waterway downstream the Yangtze River. *Port & Waterway Engineering*, 159-164.

Nones, M., Archetti, R., Guerrero, M. (2018). Time-Lapse Photography of the Edge-of-Water Line Displacements of a Sandbar as a Proxy of Riverine Morphodynamics. *Water*, 10, 617.

Parsons, D.R., Best, J.L., Lane, S.N., Orfeo, O., Hardy, R.J., Kostaschuk, R. (2007). Form roughness and the absence of secondary flow in a large confluence–difffluence, Rio Paraná, Argentina. *Earth Surface Processes and Landforms: The Journal of the British Geomorphological Research Group*, 32, 155-162.

Peng, B., Xie, C., Huang, H., Wu, T. (2018). Research on numerical simulation of water flow characteristics in Heishazhou waterway of Yangtze River. *Yangtze River*, 49, 1-5. (In Chinese).

Provansal, M., Dufour, S., Sabatier, F., Anthony, E.J., Raccasi, G., Robresco, S. (2014). The geomorphic evolution and sediment balance of the lower Rhône River (southern France) over the last 130 years: Hydropower dams versus other control factors. *Geomorphology*, 219, 27-41.

Rhoads, B.L., Kenworthy, S.T. (1995). Flow structure at an asymmetrical stream confluence. *Geomorphology*, 11, 273-293.

Schmidt, J.C., Wilcock, P.R. (2008). Metrics for assessing the downstream effects of dams. *Water Resources Research*, 44.

Seminara, G., Tubino, M. (1989). Alternate bars and meandering: free, forced and mixed

interactions. *River meandering*, 12, 267-320.

Szupiany, R., Amsler, M., Hernandez, J., Parsons, D., Best, J.L., Fornari, E., Trento, A. (2012). Flow fields, bed shear stresses, and suspended bed sediment dynamics in bifurcations of a large river. *Water Resources Research*, 48.

Szupiany, R.N., Amsler, M.L., Parsons, D.R., Best, J.L. (2009). Morphology, flow structure, and suspended bed sediment transport at two large braid-bar confluences. *Water Resources Research*, 45.

Thomas, R.E., Parsons, D.R., Sandbach, S.D., Keevil, G.M., Marra, W.A., Hardy, R.J., Best, J.L., Lane, S.N., Ross, J.A. (2011). An experimental study of discharge partitioning and flow structure at symmetrical bifurcations. *Earth Surface Processes and Landforms*, 36, 2069-2082.

Thompson, D.M. (2011). The velocity-reversal hypothesis revisited. *Progress in Physical Geography*, 35, 123-132.

Thorne, C.R., Zevenbergen, L., Pitlick, J., Rais, S., Bradley, J., Julien, P. (1985). Direct measurements of secondary currents in a meandering sand-bed river. *Nature*, 315, 746.

Tubino, M., Repetto, R., Zolezzi, G. (1999). Free bars in rivers. *Journal of Hydraulic Research*, 37, 759-775.

Van Denderen, R.P., Schielen, R.M., Blom, A., Hulscher, S.J., Kleinhans, M.G. (2018). Morphodynamic assessment of side channel systems using a simple one-dimensional bifurcation model and a comparison with aerial images. *Earth surface processes and landforms*, 43, 1169-1182.

Wu, F.C., Yeh, T.H. (2005). Forced bars induced by variations of channel width: Implications for incipient bifurcation. *Journal of Geophysical Research: Earth Surface*, 110.

Xia, J., Zhou, M., Lin, F., Deng, S., Lu, J. (2017). Variation in reach-scale bankfull discharge of the Jingjiang Reach undergoing upstream and downstream boundary controls. *Journal of hydrology*, 547, 534-543.

Xu, J. (1989). COMPLEX RESPONSE IN THE CHANNEL ADJUSTMENT OF THE LOWER WEIHE RIVER TO THE CONSTRUCTION OF THE SANMENXIA RESERVOIR. *Geographical Research*, 8, 82-90.

Yang, Q.Y., Wang, X.Y., Lu, W.Z., Wang, X.K. (2009). Experimental Study on Characteristics of Separation Zone in Confluence Zones in Rivers. *Journal of Hydrologic Engineering*, 14, 166-171.

Yang, S.L., Milliman, J.D., Xu, K.H., Deng, B., Zhang, X., Luo, X. (2014). Downstream sedimentary and geomorphic impacts of the Three Gorges Dam on the Yangtze River. *Earth-Science Reviews*, 138, 469-486.

Yi, Y.-j., Zhang, S.-h., Wang, Z.-y. (2013). The bedform morphology of Chinese sturgeon spawning sites in the Yangtze River. *International Journal of Sediment Research*, 28, 421-429.

Zhou, M., Xia, J., Lu, J., Deng, S., Lin, F. (2017). Morphological adjustments in a meandering reach of the middle Yangtze River caused by severe human activities. *Geomorphology*, 285, 325-332.

Zinger, J.A., Rhoads, B.L., Best, J.L., Johnson, K.K. (2013). Flow structure and channel

morphodynamics of meander bend chute cutoffs: A case study of the Wabash River, USA. *Journal of Geophysical Research: Earth Surface*, 118, 2468-2487.